

This is the accepted manuscript made available via CHORUS. The article has been published as:

Biaxial strain effects on adatom surface diffusion on tungsten from first principles

Zhengzheng Chen and Nasr Ghoniem

Phys. Rev. B **88**, 035415 — Published 9 July 2013

DOI: [10.1103/PhysRevB.88.035415](https://doi.org/10.1103/PhysRevB.88.035415)

Biaxial strain effects on adatom surface diffusion in tungsten from first principles

Zhengzheng Chen and Nasr Ghoniem

Department of Mechanical and Aerospace Engineering, University of California Los Angeles, CA 90095

(Dated: June 26, 2013)

Using first-principles electronic structure calculations, the energy barriers for diffusion mechanisms of adatoms on the tungsten (W) (001) and (110) surfaces under externally-applied biaxial strain fields are determined. Adatoms move either by hopping on the surface or by an exchange process with a surface atom, which is found to be completed in one step (direct exchange), or via the formation of a surface crowdion (crowdion-mediated exchange). As a result of the compact atomic stacking, hopping is found to be the major diffusion mechanism on the W(110) surface, irrespective of the surface strain state. On the other hand, the main diffusion mechanism on the less compact W(001) surface is found to be a competition between direct *exchange* and *crowdion-mediated exchange*, depending on the magnitude of the surface biaxial strain. Results of the model reveal that, if surface crowdions form, they will be highly mobile and migrate anisotropically. A microscopic explanation is presented by analyzing the charge density associated with surface crowdions. A “mechanism diagram” for atomic surface diffusion on the W(001) indicates that the diffusion direction and its rate can both be modulated by an applied biaxial strain. Migration volumes for the three mechanisms are calculated, and the significance of the results to the understanding of surface evolution under plasma or other energetic ion bombardment is highlighted.

PACS numbers: 82.20.Db, 71.15.Mb, 68.43.Mn

I. INTRODUCTION

The fundamental nature of the effects of stress on the diffusion of surface atoms has great consequences in many applied research areas. The influence of external strain fields on atomic mobility have been observed in both simulations and experiments^{1–8}. This coupling between the strain-field and atomic migration barriers has been well recognized in a variety of surface processes, e.g., self-assembly of nano-clusters, growth of thin films, surface instabilities, etc.^{9,10}. For instance, Zhu *et al* reported kinetic Monte-Carlo simulations on the effects of surface strain on the growth of quantum dots⁵. Panat *et al* also studied the evolution of surface waviness modulated by surface strain⁶. These studies show that it is necessary to have a full understanding of the effects of the surface stress state on atomic diffusion in order to build up comprehensive models that describe the dynamics of surface evolution.

The refractory nature of W and its high melting point makes it a candidate for scientific and applied studies of materials operating in extreme conditions. The metal has attracted recent intensive attention as a candidate plasma-facing material, serving in fusion and plasma devices. Its low sputtering yield when bombarded with low energy ions makes it suitable for many plasma-device applications^{11–13}, as well as in applications in emerging space electric propulsion and pulsed power systems¹⁴. Because W will be subjected to high-dose bombardment of low-energy ions in this wide range of applications, ion-induced surface damage and subsequent morphological evolution are of great concern. Experiments have established that when W is exposed to low-energy plasma ions (e.g. a high-flux of deuterium plasma¹⁵), significant microstructure and morphology changes take place in the

near-surface region. The interaction of energetic photons, electrons, and ions with the W surface results in a rich variety of phenomena. At low deposition power, the material is heated with an accompanying thermal stress. As power is increased, and depending on the intensity of deposition, a variety of phenomena take place in the solid state, such as plastic deformation, bulk and surface diffusion, and phase transformations. When these mechanisms are operative in the solid state, the material’s surface is no longer static, but it undergoes dynamic morphological changes in response to this type of intense energy input. Surface features under these conditions include cracks, extrusions, cones, islands, hillocks, and whiskers. In low energy plasma devices, ion and neutral energies in the range of 10-100 eV penetrate only several to tens of atomic layers, causing significant sputtering of surface layers. Because of the shallow depth of penetration, most of the implanted ions (e.g. He, H, Ar, Xe) are insoluble in the material and tend to agglomerate in nanoscale bubbles that cause blisters and surface exfoliation. The interaction of fast ions with a solid surface will lead to material removal and transport throughout the system through physical sputtering¹⁶ and exfoliation¹⁷. At room temperature, blistering¹⁸ occurs in all noble gas implanted materials. For example, at a He ion fluence of $3 \times 10^{21}/\text{m}^2$ blistering starts to take place, and exfoliation occurs at a fluence around $10^{22}/\text{m}^2$ ^{19,20}. Tokitani *et al* reported the formation of fine helium bubbles and the essential decrease of density of W matrix due to void swelling after high fluence of helium irradiation^{21,22}. The local surface stress state in the vicinity of sub-surface bubbles and other defect clusters may be compressive or tensile, depending on the elastic properties of the defect inclusion, which, in turn, is expected to influence local material flow through diffusion mechanisms.

Vast experimental observations suggest that ion bom-

bardment results in the formation of near-surface point defects, which serve as the primary medium of surface morphological instabilities through two- and/or three-dimensional migration. Central to understanding such surface evolution process is the development of a clear picture of how atoms diffuse on the W surface under these conditions. Over the past decade, numerous studies have focused on defect physics in bulk tungsten^{23–28}. As an instance, Becquart and Domain calculated migration energy and binding energy of helium atom/cluster in W²⁹. Based on this energetic scenario, they explained the tendency of He blisters formation close to the W surface. Recent studies have also provided detailed information on atomic processes on the W(110) surface^{30–33}. However, an understanding of the mechanisms of self-diffusion on the W(001) surface under an applied stress field is lacking, although some studies report the migration barrier on a stress-free surface^{34,35}. Because these studies have been carried out with empirical potentials, and because they show discrepancies of more than 1 eV in calculated diffusion energy barriers, more reliable methods are needed. All available data on atomic surface diffusion in W have been carried out for stress-free surfaces, which is a condition rarely attainable under ion or plasma bombardment. The objective of the present work is to determine the migration energy barriers of surface atoms in W under external loading so as to understand the diffusion mechanisms that lead to surface evolution in future dynamical models. We employ here first-principles methods to study the atomic migration paths on the W(001) and the W(110) surfaces under external biaxial strains. The paper is organized as follows: in Sec. II, we briefly summarize the calculation model and methodology. Detailed results and a discussion of typical atomic migration paths under biaxial strains on both (001) and (110) surfaces are presented in Sec. III and Sec. IV, respectively. Finally, summary and conclusions are given in Sec. V.

II. MODEL AND METHODOLOGY

We will consider here three possible migration mechanisms of an adatom that can result in self-diffusion on W(001) and W(110) surfaces: (1) hopping (H), (2) simple exchange (Ex), and (3) crowdion-mediated exchange. In the hopping mechanism, adatoms move from one low energy position to an identical position on the surface by executing motion through a bridge site (saddle point). In the exchange mechanism, adatoms are embedded into the surface layer, and then get replaced by ejection of a *different* surface atom that would reside in a position identical to that of the original adatoms. Thus, the initial and final configuration of the adatom and atomic lattice look the same, but with a different adatom on the surface. Evidently, this scenario works only for self-diffusion. The interesting aspect of the exchange mechanism is that if the adatom pops out a lattice atom in one single step, one would describe this mechanism as “simple

exchange.” However, the possibility exists that once the adatom embeds itself into the surface layer, a crowdion configuration involving several surface atoms may form, and at some distance from the original event, one of the atoms forming the crowdion row may pop out on the surface again to replicate the initial configuration of the adatom itself. This is crowdion-mediated exchange mechanism. Clearly, this mechanism consists of two different events: the conversion between adatoms and crowdions ($A \rightarrow C$ or $C \rightarrow A$), and crowdions migration ($C \rightarrow C$).

In an earlier study, Feibelman examined the mobility of adatoms on the Al (100) surface via a “replacement” mechanism involving a dimer, rather than the much studied hopping mechanism across atomic ridges on fcc metal surfaces³⁶. More recently, Xiao and Chrzan^{1,2} extended the replacement concept to describe adatom diffusion on Cu surfaces via surface crowdions by performing nudged elastic band (NEB) calculations using the Embedded Atom Method (EAM). Their study concluded that diffusion on strained Cu is mediated by the formation and motion of a surface crowdion. The high mobility of crowdions has also been reported for several metals^{37–39}. In the present investigation, we explore the dominant diffusion mechanisms on W(001) and W(110) surfaces with more precise first-principles calculations in order to reveal the electronic origin of the effects of an applied strain field on adatom motion. Fig. 1(a) and (b) show the atomic configurations of paths H, Ex, $A \rightarrow C$ and $C \rightarrow C$ on the W(001) and W(110) surfaces. We only focus on [100]-crowdions on the W(001) and $\bar{1}11$ -crowdions on the W(110) surfaces, because they are the most stable crowdion configurations. The notation we will use henceforth is as follows: a superscript * is used to indicate the energy barrier, and a subscript “H”, “Ex”, “ $A \rightarrow C$ ” or “ $C \rightarrow C$ ” is used for different diffusion mechanisms, respectively. The crystallographic direction of diffusion motion will also be attached as an additional subscript. Thus, $E_{A \rightarrow C[100]}^*$ is the energy barrier of forming a [100]-crowdion from an adatom.

A strain tensor is applied on the computational cell as⁴⁰: $\varepsilon_{33} = \varepsilon_{12} = \varepsilon_{13} = \varepsilon_{23} = 0$, while ε_{11} and ε_{22} are independently changed from -0.02 to 0.02. Since we chose orthogonal supercells, we simply change the lengths of a $N_1 \times N_2$ supercell along the [100] and [010] directions as $a_1 = a^0 \varepsilon_{11}$, and $a_2 = a^0 \varepsilon_{22}$, where $a^0 = 3.165$ Å is the strain-free single lattice constant, and a_1, a_2 are the corresponding strained lattice constant.

First-Principles calculations were performed with the Vienna *ab-initio* simulation package (VASP)^{41,42}. The Perdew-Burke-Ernzerhof generalized gradient approximation (GGA)⁴³ was employed to describe the exchange and correlation functionals. Electron-ion interactions were treated within the projected augmented wave (PAW) approach.⁴⁴ An energy cutoff of 300 eV was used for the plane-wave expansion of the wave functions. For the (001) surface, we employed a 65-atom 4×4 four-layer supercell containing an adatom or a self-interstitial atom (SIA), and a $4 \times 4 \times 1$ k -point mesh according to the

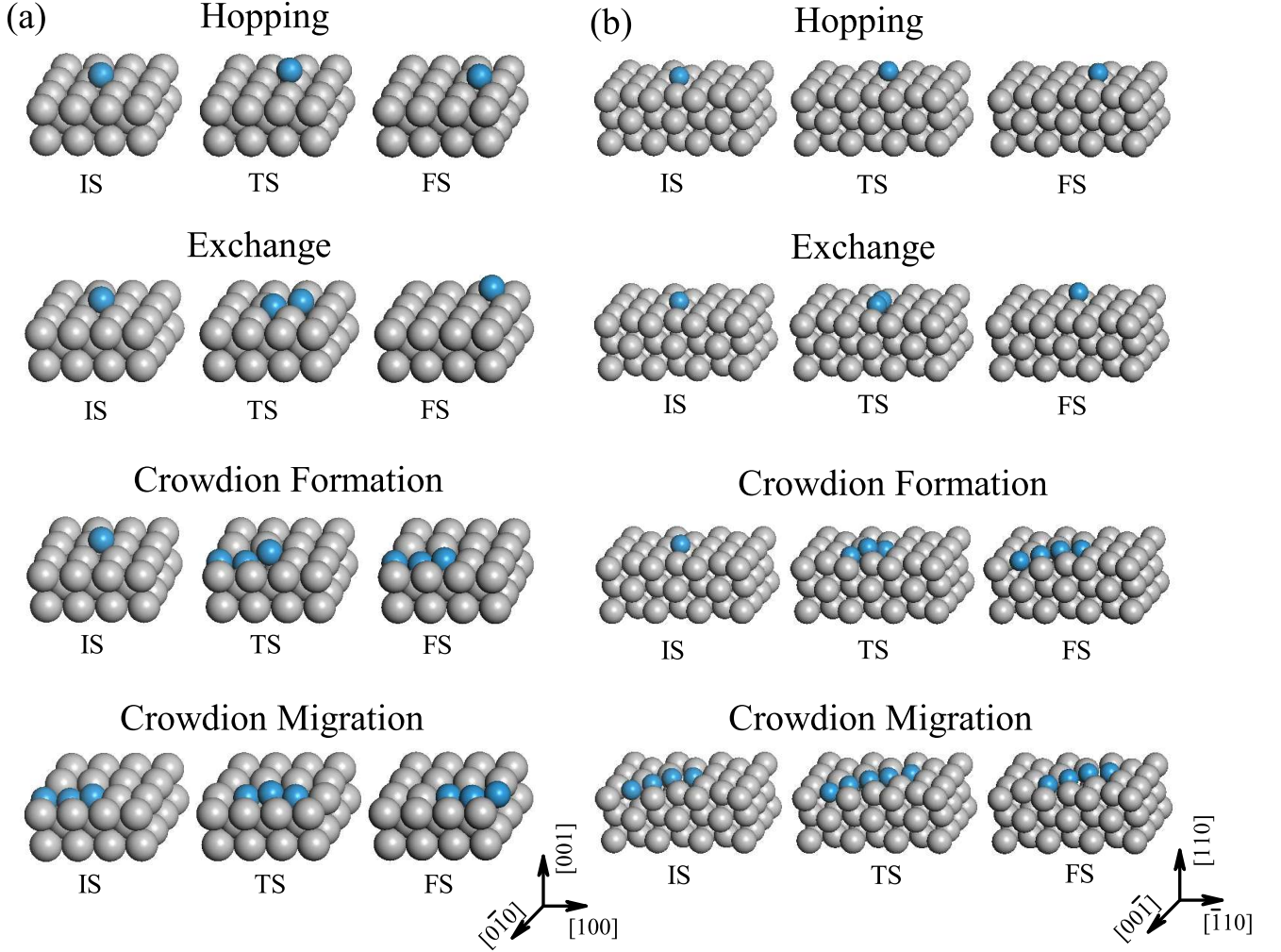


FIG. 1. (Color online) Schematic illustration of paths H, Ex, A \rightarrow C and C \rightarrow C of adatoms on (a) the W(001) and (b) the (110) surface. The migration paths of crowdions are presented as well. “IS”, “TS” and “FS” represent initial state, transition state and final state, respectively. Most involved atoms are highlighted as blue spheres, all other atoms are shown in grey.

Monkhorst-Pack (MK) scheme.⁴⁵ For the (110) surface, a 73-atom 3×3 four-layer supercell with an adatom/SIA and a $4\times 6\times 1$ MK k -point mesh have been employed. Methfessel-Paxton broadening scheme is used for Brillouin zone integration with smear width as 0.05 eV for both surfaces. These settings yield an energy convergence of less than 3 meV/atom. Under each biaxial strain, optimized atomic geometries are achieved when forces on all unconstrained atoms on the top three layers are smaller in magnitude than 0.02 eV/Å.

Since surface crowdions induce atomic displacements, we have checked the convergence of the supercell size. For the W(001) surface, under zero strain, the [100]-crowdion only affects three nearest atoms. The displacement of the atom at the boundary of the supercell is less than 0.015 Å. We further used a 6×4 supercell to calculate the $E_{C\rightarrow C[100]}^*$ as 0.189 eV, where for the current 4×4 supercell, =0.184 eV. Similar discussions are valid for

W(110) surfaces as well. When the $[\bar{1}11]$ -crowdion is at the center of the 3×3 supercell, the biggest displacement of the boundary atoms is 0.015 Å. By using a 5×4 supercell, we obtained $E_{C\rightarrow C[100]}^*$ as 0.111 eV, only 4 meV lower than the result with the 3×3 supercell. Displacements of the outermost atoms and migration barriers both suggest that convergence has been achieved by current supercells.

Surface diffusion can be described by a “diffusion strain tensor”, which is defined as⁴.

$$V_{ij}^* = -\frac{\partial R}{\partial \sigma_{ij}} = \Omega_0 \int_{AX}^{AX^*} d\varepsilon_{ij} \quad (1)$$

where Ω_0 is the atomic volume under zero strain, R is the work done on moving the atom from the equilibrium state (AX) to the activated state (AX^{*}). This is only a component of the “activation” volume tensor, in case the defect requires a formation energy ($V^{act} = V^f + V^*$)⁴. The exact amount of additional work requires knowledge

of the lattice deformation around the adatom during its motion. In general, the additional work is a non-linear function of external stress (or strain)¹. However, and as an approximation, the migration energy was proposed to have the simpler form⁴⁶ that depends only on the start (minimum energy) and saddle points, and not on the details of the path:

$$E^*(\sigma) = E_0^* + \Omega \Delta \sigma : \varepsilon \quad (2)$$

$\Delta \sigma = \sigma^{\text{sad}} - \sigma^{\text{min}}$, and σ^{sad} and σ^{min} are the surface-stress tensors induced by the adatom at the saddle and minimum point, respectively⁴⁷. The migration energy on the unstrained surface (E_0^*) is changed by adding the work done by the adatom during its motion from the minimum energy position to the saddle point. Since the adatom induces surface stress as it deforms the lattice when it moves, the term $\Omega \Delta \sigma$ may be interpreted as a scaled average force experienced by the adatom during the transition. When an applied strain is introduced, an additional amount of work will be done by this average force against the applied strain. Since the applied strain is linear with the stress, the migration energies, $E_{\text{H}}^*(\varepsilon_{11}, \varepsilon_{22})$ and $E_{\text{Ex}}^*(\varepsilon_{11}, \varepsilon_{22})$, for adatoms on tungsten surfaces were fitted to a model that allows extraction of a migration volume tensor, as the strain-conjugate of energy (Eq. 1)⁴:

$$E^*(\sigma) = E_0^* + \mathbf{V}^m : \sigma \quad (3)$$

where \mathbf{V}^* is the migration volume tensor defined by Eq. 1. This was further simplified by considering only in-plane normal strain components. Thus, only the two components, V_{11}^* and V_{22}^* of the migration volume are recovered in the present work. Since we apply strains and not stresses, we used the elastic constants of W to obtain the migration volume by using $\sigma = \mathbf{C} : \varepsilon$, in which the elastic constants tensor \mathbf{C} is taken from Ref.⁴⁸. The NEB method^{49,50} was used to determine the migration barrier of atomic migration paths under different biaxial strains. We performed several tests, and found that Path-H and Path-Ex are easy to converge to their minimum energy paths (MEPs), while Path-AC and Path-CC are relatively more difficult to get convergence. Therefore, and based on careful tests, we have used three (six) replicas between the initial and final geometries for hopping and exchange (formation and movement of crowdions) paths on both surfaces to produce a smooth MEP. The convergence criterion is that all forces on unconstrained atoms are less than 0.03 eV/Å.

III. RESULTS AND DISCUSSION

A. Adatom Migration Energy on the (001) surface

The saddle point migration energies E_{H}^* , E_{Ex}^* and $E_{\text{A} \rightarrow \text{C}}^*$ as functions of $(\varepsilon_{11}, \varepsilon_{22})$ are presented in Fig. 2(a) for adatoms on the W(001) surface. In order to show

the results more quantitatively, we also present three plots of E^* as function of ε_{11} , with ε_{22} held constant at -0.02, 0.0, and 0.02 in Figs. 2(b)-(d), respectively. Surprisingly, under zero strain, a W adatom prefers to be incorporated into the surface layer and form a [100]-crowdion, for which $E_{\text{A} \rightarrow \text{C}}^*$ is 1.57 eV; lower than E_{Ex}^* and E_{H}^* by ≈ 0.27 eV and 0.90 eV, respectively. The relaxed atomic structure shows that the [100]-crowdion has a tilt axis making an angle of 12° from the [100]-direction and out of the (001) surface. This suggests that the out-of-plane displacement of the crowdion effectively decreases its migration energy, facilitating its surface motion. Note that E_{Ex}^* is also 0.66 eV lower than E_{H}^* . Therefore, on this less tightly-packed (001)-surface, surface self-diffusion occurs mainly by exchanging adatoms with surface atoms. Fig. 2(a) also shows that an applied biaxial strain makes it possible to modulate the energetically favorable migration paths. Under extreme biaxial strains of $\varepsilon_{11} = -\varepsilon_{22} = -0.03$, $E_{\text{A} \rightarrow \text{C}}^*$ is higher than E_{H}^* so crowdion migration becomes the least favorable path. More importantly, a transition takes place along the load line $-15.91\varepsilon_{11} + 6.99\varepsilon_{22} = 0.27$, since the dominant migration mode switches between the exchange and crowdion mechanisms.

Figs. 2(b)-(d) show the relationship among the three migration mechanisms. When the W(001) surface is compressed along the [010]-direction, E_{H}^* is the highest (least probable migration mechanism). As ε_{22} increases from compression to tension, however, the migration barriers of the other two mechanisms start to increase. Additionally, with a compressive strain of $\varepsilon_{22} = -0.02$, crowdion migration remains as the dominant mechanism for $\varepsilon_{11} > -0.025$. When ε_{22} increases, the favorable mechanism converts to the exchange mechanism under smaller compression along the [100]-direction. Fig. 2 also shows the asymmetric relative ordering of the migration barriers to applied external strains, ε_{11} and ε_{22} . For instance, $E_{\text{H}}^*(0.02, 0.0)$ is 0.51 eV higher than $E_{\text{H}}^*(-0.02, 0.0)$, while $E_{\text{H}}^*(0.0, 0.02)$ is only 0.16 eV higher than $E_{\text{H}}^*(0.0, -0.02)$. Interestingly, $E_{\text{A} \rightarrow \text{C}}^*$ shows the opposite behavior: it increases with compression along the [100]-direction, while it decreases with compression along the [010]-direction. The former feature is straightforward, since compression along the [100]-direction decreases the available volume for forming a [100]-crowdion. Although the crowdion tilt axis is at 17° for $\varepsilon_{11} = -0.02$, facilitating elastic energy release, $E_{\text{A} \rightarrow \text{C}}^*$ increases still with increasing compression. In order to understand this latter feature, we analyze the distance between the top layer and sub-surface layer $d_{12}^{(001)}$ for various ε_{22} . Compared to the zero-strain case, $d_{12}^{(001)}$ decreases when $\varepsilon_{22} > 0$, and increases when $\varepsilon_{22} < 0$. When $d_{12}^{(001)}$ decreases, surface atoms interact stronger with the sub-surface layer. Consequently, when an adatom is incorporated into the surface with $\varepsilon_{22} > 0$, it costs more energy to push nearby atoms. As shown in Fig. 2, both E_{H}^* and E_{Ex}^* increase in the tensile region as well, which can be explained in a similar fashion.

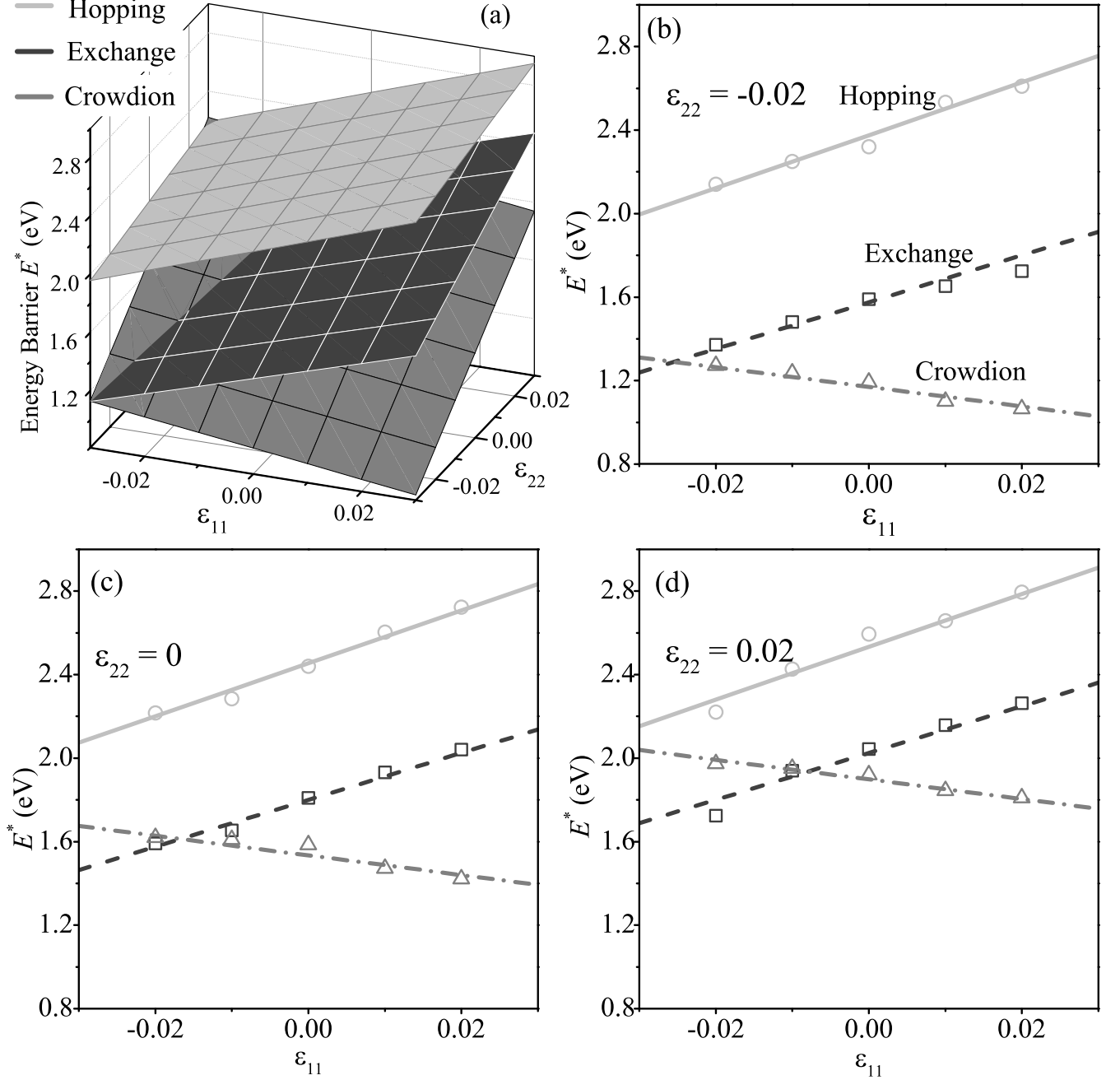


FIG. 2. (a) $E_H^*(\epsilon)$, $E_{Ex}^*(\epsilon)$ and $E_{A \rightarrow C}^*(\epsilon)$ on the W(001) surface. (b)-(d) Slices with $\epsilon_{22} = -0.02, 0.0$, and 0.02 , respectively. E_H^* , E_{Ex}^* and $E_{A \rightarrow C}^*$ are represented by the solid light gray line, the dashed dark gray line, and the dot-dash gray line, respectively. Symbols represent calculated energy barriers by NEB method.

One should note, however, that E_{Ex}^* dependence on ϵ_{11} and ϵ_{22} has 90° rotational invariance on the (100)-plane, while E_H^* shows apparent anisotropy. This is because Path-Ex is along the $[110]$ -direction, which is symmetric with respect to ϵ_{11} and ϵ_{22} , while Path-H is along the $[100]$ -direction, and thus positive ϵ_{11} raises E_H^* more by elongating the hopping distance of Path-H.

Based on Eq. (3), we fitted the migration barriers to

the applied stress tensor to obtain the two diagonal elements of the migration volume tensor: \mathbf{V}^* , which is an important parameter to describe surface diffusion under external loading. The results are listed in Table I. \mathbf{V}^* shows the anisotropy of migration paths more clearly: E_H^* and $E_{A \rightarrow C}^*$ both have V_{11}^* and V_{22}^* with opposite signs, while for E_{Ex}^* , $V_{11}^* = V_{22}^*$. Note that: (1) though Path-H and Path-A \rightarrow C are both along $[100]$, the signs of the

TABLE I. $E_H^*(0)$, $E_{Ex}^*(0)$, $E_{A \rightarrow C}^*(0)$ and migration volume tensor components on the W(001) and the W(110) surfaces under biaxial strains. The unit of the energy barrier is eV, and that of the migration volume is \AA^3 . Note that σ_{11} is in the units of $\text{eV}/\text{\AA}^3$.

	(001)			(110)		
	H	Ex	A \rightarrow C	H	Ex	A \rightarrow C
E_0^*	2.47	1.81	1.54	0.87	3.09	4.68
V_{11}^*	4.02	2.49	-4.23	$-0.58 + 8.28\sigma_{11}$	-0.19	-7.79
V_{22}^*	-0.34	2.49	7.23	0.73	-1.04	-5.42

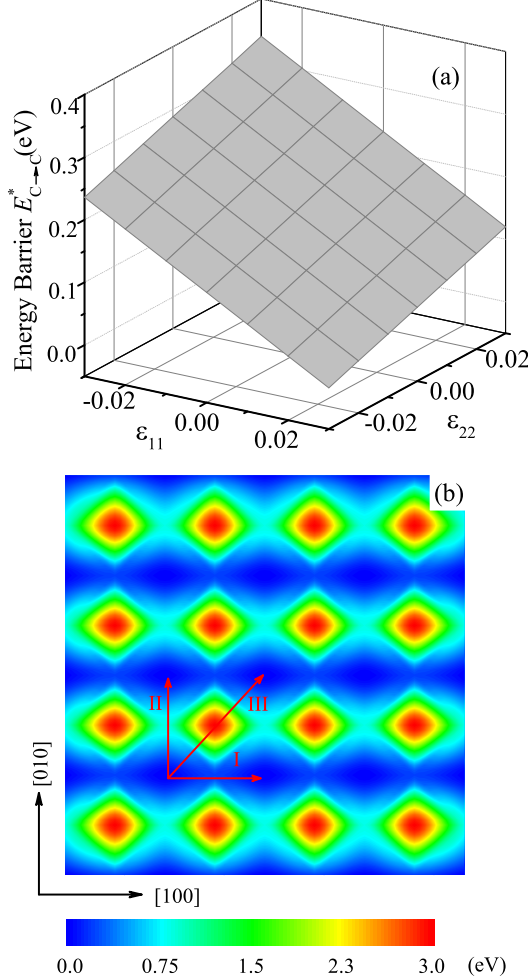


FIG. 3. (Color online) top panel: $E_{C \rightarrow C}^*(\epsilon)$ of the [100]-crowdion on the W(001) surface. bottom panel: PES of the [100]-crowdion, which indicates strong one-dimensional motion.

corresponding migration volumes V_{11}^* (V_{22}^m) are opposite; and (2) Path-A \rightarrow C is along [100], but its migration volume $|V_{11}^*|$ is smaller than V_{22}^* . These results are consistent with the above discussion, and suggest that the orientation of a migration path affects the anisotropy of the corresponding migration energy barrier E^* , resulting in significant overall surface diffusion anisotropy.

B. Crowdion Migration Energy in the (001) surface

The conversion of a crowdion into an adatom is energetically favorable, and will thus be an intermediate state for adatom diffusion. However, it is possible that crowdions may form in the surface or near surface layers as “interstitials” resulting from energetic ion interaction with surface layers. In this case, and similar to a Self Interstitial Atom (SIA) in the bulk of irradiated crystals⁵¹, such surface crowdions may be able to move long distances with a small energy barrier before conversion to an adatom. We thus calculated the migration barrier of the [100]-crowdion, $E_{C \rightarrow C[100]}^*$, under biaxial strain. Similarly, we also fitted $E_{C \rightarrow C[100]}^*$ to a linear function of strain to enable extraction of a migration energy activation volume.

$$E_{C \rightarrow C[100]}^*(\epsilon) = 0.19 - 3.67\epsilon_{11} + 1.74\epsilon_{22} \quad (4)$$

Fig. 3(a) shows the dependence of $E_{C \rightarrow C[100]}^*(\epsilon)$ on the external biaxial strain, similar to $E_{A \rightarrow C}^*$ (shown in Fig. 2), but with a smaller change. With an increase in ϵ_{11} , and although the migration distance is longer, the [100]-crowdion axis has a smaller tilt angle (8° at $\epsilon_{11} = 0.02$), and therefore its migration path along the [100]-direction is less wavy. Furthermore, there exists a larger available volume to regenerate a crowdion at larger values of ϵ_{11} . Both factors lower the migration energy barrier. Note that $E_{C \rightarrow C[100]}^*$ is only 0.19 eV at $\epsilon = 0$; much smaller than the barriers of the aforementioned three adatom migration mechanisms. One can conclude that once a surface crowdion forms, it will travel very fast and, will thus greatly enhance surface diffusion.

We also studied the dimensionality of the [100]-crowdion diffusion. As shown in Fig. 3(b), three migration paths, along [100], [010], and [110] were considered. The results of migration along [100] are shown in Eq. (4), and Fig. 3(a). Along [010], the TS is similar to that of Path-H, while $E_{C \rightarrow C[100]}^*$ is 0.85 eV. NEB calculations demonstrate that [110] migration is physically unstable. The migrating atom prefers to be an adatom somewhere during migration in the middle of the path. Therefore, [110]-migration will spontaneously decompose into a two-step process, namely, *crowdion* \rightarrow *adatom* \rightarrow *crowdion*. We artificially assigned $E_{C \rightarrow C}^*$ along [010] a large value in order to indicate that the crowdion will not choose to migrate along this direction. Based on the above discussions, we present the potential energy surface (PES) of the [100]-crowdion in Fig. 3(b). Clearly, migration of the [100]-crowdion displays very strong anisotropy, and should be viewed to move essentially as a one-dimensional particle in future dynamical models of surface evolution.

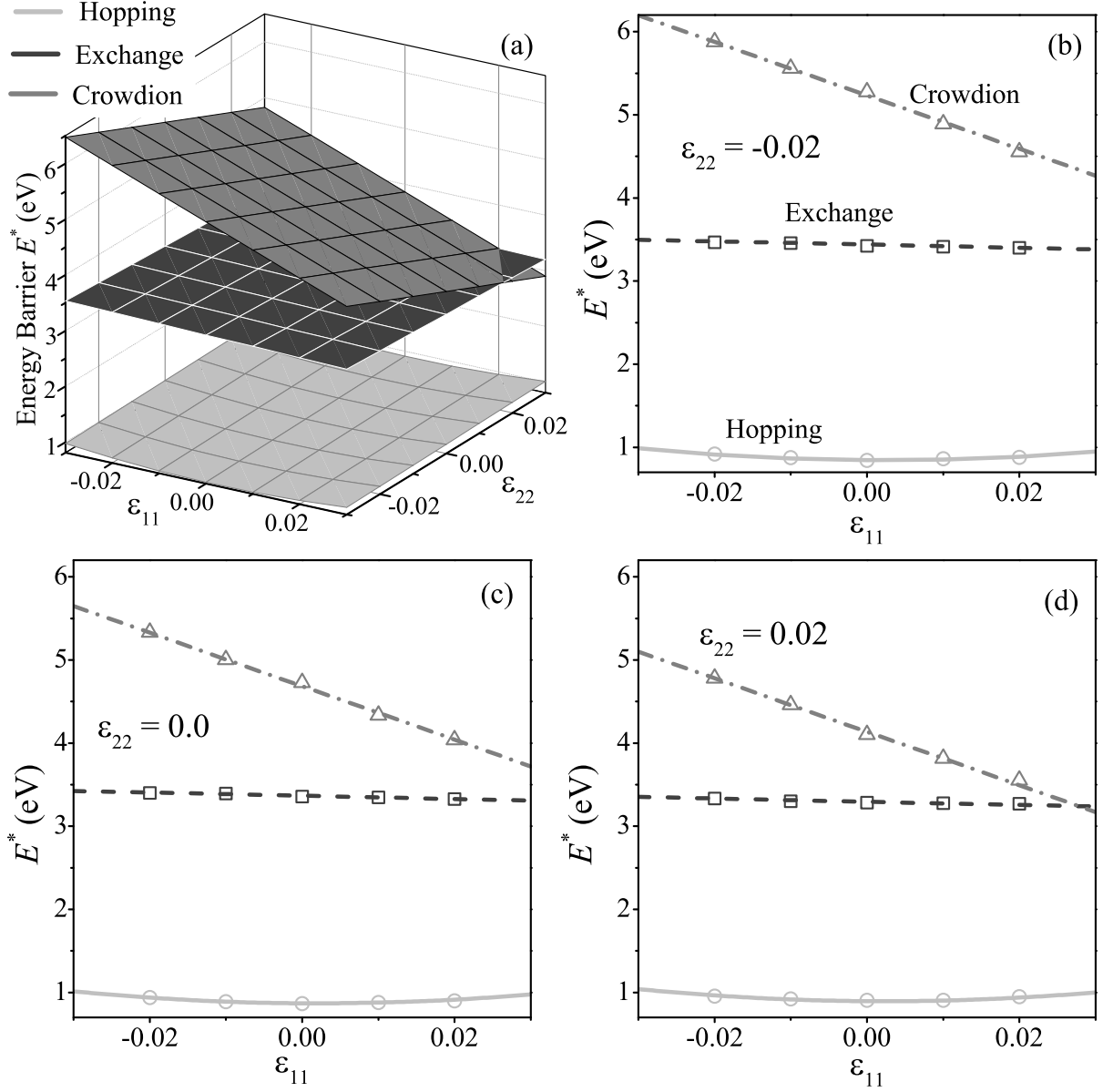


FIG. 4. (a) $E_H^*(\epsilon)$, $E_{Ex}^*(\epsilon)$ and $E_{A \rightarrow C}^*(\epsilon)$ on the W(110) surface. (b)-(d), 2-D Slices with $\epsilon_{22} = -0.02, 0.0$, and 0.02 , respectively. E_H^* , E_{Ex}^* , and $E_{A \rightarrow C}^*$ are represented by the solid light gray line, the dashed dark gray line, and the dot-dash gray line, respectively. Symbols represent calculated energy barriers by NEB method.

C. Adatom Migration Energy on the (110) surface

Fig. 4 shows E_H^* , E_{Ex}^* and $E_{A \rightarrow C}^*$ on the W(110) surface. Calculated migration volumes for each path are given in Table I. Comparing to Fig. 2, it is clear that adatom diffusion on the W(110) surface displays opposite scenarios from the W(001) surface. E_H^* is much lower than E_{Ex}^* and $E_{A \rightarrow C}^*$, regardless of the biaxial strain. Under zero strain, E_H^* on the (110) surface is only 0.87 eV, which is in good agreement with the previous result of 0.90 eV^{32,52,53}, and slightly lower than the recent measurement of 0.94 eV^{33,54}. E_{Ex}^* and $E_{A \rightarrow C}^*$ are much

higher, being 3.09 eV and 4.68 eV, respectively. This large difference can be attributed to the fact that the (110) surface is the compact plane of tungsten. Also, the (110) surface has the largest inter-planar distance. Therefore the Path-H has a very short hopping distance ($\sqrt{2}/2a_0$), and will experience a weak adatom-surface interaction. On the other hand, the available atomic volume is small in the (110) top layer. Path-A \rightarrow C thus has to overcome larger elastic energy. As shown in Fig. 4, $E_{A \rightarrow C}^*$ is sensitive to the external loading. It increases to 6.47 eV with $\epsilon_{11} = \epsilon_{22} = -0.03$, and decreases to 2.90 eV with $\epsilon_{11} = \epsilon_{22} = 0.03$. Correspondingly, $E_{A \rightarrow C}^*$ has the

largest \mathbf{V}^* (See Table I). Furthermore, different from its counterpart on the W(001) surface, both components of \mathbf{V}^* of $E_{A \rightarrow C}^*$ are negative. Since the $[\bar{1}11]$ -crowdion has components along both $[\bar{1}10]$ and $[001]$ directions, elongation along any direction will increase the atomic volume for the crowdion, and is thus beneficial to lowering the barrier. On the other hand, E_{Ex}^* is almost independent of ε , which causes the intersection with $E_{A \rightarrow C}^*$ in the extreme tensile region. However, this intersection does not change the dominant role of Path-H because of the much lower E_H^* .

Surprisingly, we have found that E_H^* does not change monotonically with ε_{11} : it decreases in compression ($\varepsilon_{11} < 0$), but increases with tension ($\varepsilon_{11} > 0$). The best fitting of E_H^* shows as a concave parabolic cylinder. As shown in Table I, V_{11}^* is not a constant, but a linear function of stress σ_{11} . Furthermore, both components of \mathbf{V}^* are small, so that E_H^* is not apparently affected by the external strain, which is similar to E_{Ex}^* . The non-linear feature of E_H^* suggests that Path-H depends on the status of strain. We have used two factors to describe Path-H, which are the distance between the adatom and surface at TS d_{a-s}^{TS} and that at IS d_{a-s}^{IS} . According to the structure analysis, both d_{a-s}^{TS} and d_{a-s}^{IS} decrease with ε_{11} . One plausible explanation of the quadratic behavior of E_H^* is as follows. d_{a-s}^{IS} describes the interaction between the adatom and the surface and determines the energy of IS. d_{a-s}^{TS} determines the energy of TS. These two factors work together to determine E_H^* . In the case of $\varepsilon_{11} > 0$, d_{a-s}^{IS} is more important. When ε_{11} increases, the adatom interacts stronger with the surface and thus increases E_H^* . In the case of $\varepsilon_{11} < 0$, d_{a-s}^{TS} is the dominant one. d_{a-s}^{TS} increases by increasing the compression. The energy of TS is higher, and therefore increases E_H^* .

Path-H and Path-Ex show apparent facet-dependence, where it is shown in Table I that \mathbf{V}^* s of Path-H and Path-Ex on the W(110) surface are much smaller than those on the W(001) surface. To explain this facet-dependence, we have checked the distance between the top layer and the sub-layer along $[001]$ and $[110]$ directions. $d_{12}^{(110)}$ is larger than $d_{12}^{(001)}$, the effects of the change of $d_{12}^{(110)}$ on E_H^* and E_{Ex}^* is expected to be smaller. Therefore, E_H^* and E_{Ex}^* on the W(110) surface are less sensitive to the external strain compared to their counterparts on the W(001) surface.

D. Crowdion Migration Energy on the (110) surface

Similar to the W(001) surface, we also determined the migration energy barrier of the $[\bar{1}11]$ -crowdion, $E_{C \rightarrow C[\bar{1}11]}^*$ as a function of biaxial strain. The results are plotted in Fig. 5, and fitted to the linear equation:

$$E_{C \rightarrow C[\bar{1}11]}^*(\varepsilon) = 0.11 + 1.68\varepsilon_{11} - 3.45\varepsilon_{22} \quad (5)$$

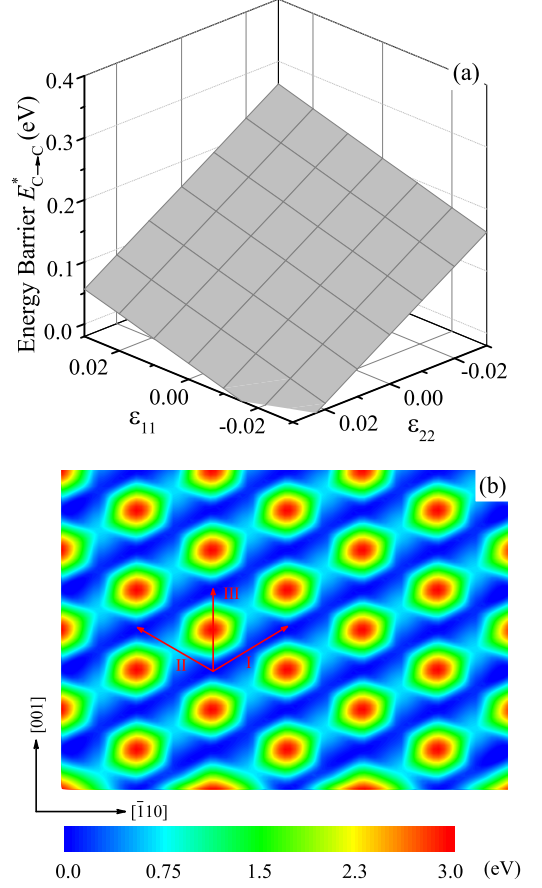


FIG. 5. (Color online) Left top: $E_{C \rightarrow C[\bar{1}11]}^*(\varepsilon)$ of the $[\bar{1}00]$ -crowdion on the W(110) surface. Bottom panel: Potential Energy Surface (PES) of the $[\bar{1}00]$ -crowdion, which indicates the one-dimensional movement of the $[\bar{1}00]$ -crowdion.

$E_{C \rightarrow C[\bar{1}11]}^*$ is only 0.11 eV, even 0.08 eV lower than $E_{C \rightarrow C[100]}^*$, which is in agreement with recent experiments by Amino *et al*²⁴. Though Eq. (5) identifies the high mobility of the $[\bar{1}11]$ -crowdion, it cannot be considered as a major carrier of diffusion on the W(110) surface under thermal conditions alone, since the very high value of $E_{A \rightarrow C}^*$ forces the generation of a $[\bar{1}11]$ -crowdion as a rare event. If these crowdions are produced by the interaction of ions with the surface layer, then their migration can be very fast. Fig. 5 also shows negative values of $E_{A \rightarrow C}^*$ if $\varepsilon_{11} < -0.015$ and $\varepsilon_{22} > 0.022$. This suggests that with such strains, the $[\bar{1}11]$ -crowdion is configured as an atomic chain along $[\bar{1}11]$ with even interatomic distances. The $[\bar{1}11]$ -crowdion can convert to an adatom at any site along the chain.

In Fig. 5(b), we also show the PES of the $[\bar{1}11]$ -crowdion. Three migration paths are illustrated. Path-I represents the intra-row migration along $[\bar{1}11]$. Path-II represents the nearest neighbor inter-row migration of the crowdion with the reorientation from $[\bar{1}11]$ to $[\bar{1}\bar{1}1]$. Path-III represents the migration along $[001]$ of the crowdion with the reorientation from $[\bar{1}11]$ to $[\bar{1}\bar{1}1]$ as well.

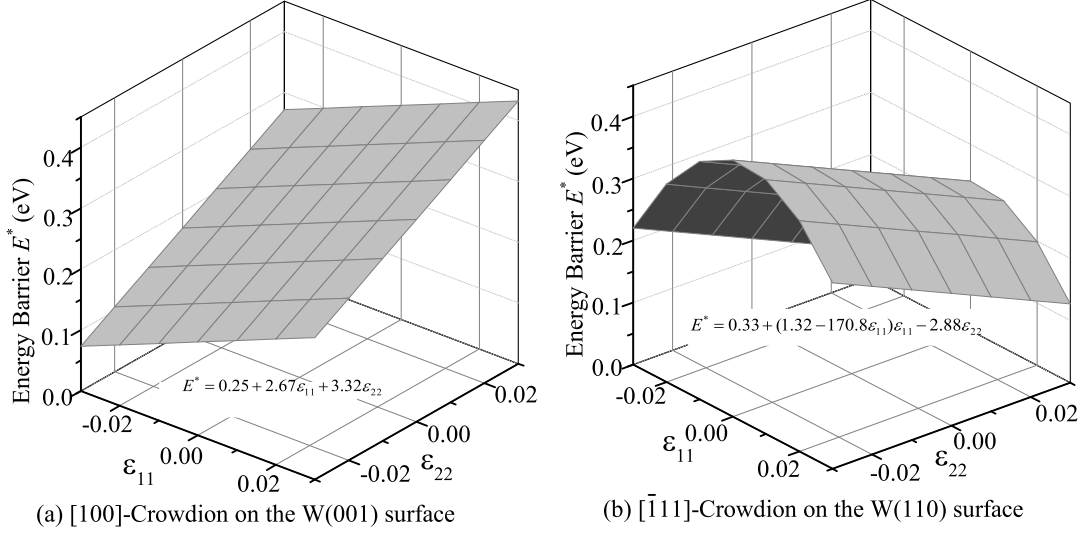


FIG. 6. (a) Energy barrier $E_{C \rightarrow A}^*(\epsilon)$ of the conversion from a [100]-Crowdion to an adatom on the W(001) surface. (b) Energy barrier $E_{C \rightarrow A}^*(\epsilon)$ of the conversion from a $[\bar{1}11]$ -Crowdion to an adatom on the W(110) surface. The best fitted equations are also shown in the figures.

Similar to the PES of the W(001) surface, anisotropy clearly appears in Fig. 5(b). $E_{C \rightarrow C}^*(\text{II})$ is 0.67 eV, six times higher than $E_{C \rightarrow C[\bar{1}11]}^*$. It is worth emphasizing that Path-III is determined to be an unstable migration path, along which the crowdion transforms to an adatom. The result is totally different from the recent report of 2.12 eV for the migration energy for the same path in bulk tungsten²⁵. Such difference between bulk and surface diffusion can be attributed to the presence of an out-of-plane degree of freedom in surface diffusion. Consequently, there is a channel along $[\bar{1}11]$ shown in Fig. 5(b), indicating essentially one-dimensional motion of the $[\bar{1}11]$ -crowdion. Because $E_{C \rightarrow C}^*(\text{II})$ is much higher than $E_{C \rightarrow C[\bar{1}11]}^*$, the crowdion is expected to migrate one-dimensionally.

E. Crowdion-to-Adatom Conversion

The crowdion configuration is not a stable one, and if a small amount of energy is acquired, it may prefer to convert to an adatom on the surface. The rate of conversion is dependent on the energy barrier for conversion, the temperature and the stress state of the surface layer. We consider here the energetics of conversion from a crowdion to an adatom on both surfaces of tungsten, and present results in Fig. 6. Equations for the best fit of the present results for $E^*(\epsilon)$ are also shown in Fig. 6.

$E_{C \rightarrow A}^*$, the barrier of conversion from a [100]-crowdion to an adatom on the W(001) surface depends linearly on ϵ_{11} and ϵ_{22} . It is much easier to convert to an adatom with biaxial compression than tension, since the available atomic volume to stabilize the [100]-crowdion is larger on

a tensile surface. On the other hand, the energy barrier of conversion from a $[\bar{1}11]$ -crowdion to an adatom on the W(110) surface shows a convex parabolic cylinder. This non-linear feature suggests that the conversion path depends on the external strain. As shown in Fig. 1(b) and Fig. 9(c), the $[\bar{1}11]$ -crowdion is not rigid along the $[\bar{1}11]$ direction. By applying an external strain, the orientation of the crowdion is changeable, making it possible to affect the conversion path from a crowdion to an adatom. One should note that $E_{C \rightarrow C[\bar{1}11]}^*$ is lower than $E_{[\bar{1}11]C \rightarrow A}^*$ within the strain range: $-0.03 \leq \epsilon_{11}, \epsilon_{22} \leq 0.03$.

Note that $E_{C \rightarrow A}^*$ and $E_{C \rightarrow C}^*$ are comparable, but have different dependance on ϵ . This fact suggests that applying external strains may be a practical way to enhance or suppress the long distance diffusion of surface crowdions. For instance, on the W(001) surface, $E_{C \rightarrow A[100]}^*$ is 0.37 eV with $\epsilon_{11} = \epsilon_{22} = 0.03$, and is only 0.14 eV with zero strain. A [100]-crowdion is therefore expected to migrate longer distance with equi-biaxial extension. Detailed discussions on long-distance diffusion are presented in Sec. IV A.

IV. DISCUSSION

A. Short and Long Distance Diffusion

To clarify the stages of adatom surface diffusion further, we show the MEPs of a complete diffusion processes in Fig. 7. Clearly, adatoms can only reach first or second nearest neighbors through Path-H or Path-Ex on both surfaces, and therefore perform short distance diffusion. On the other hand, surface crowdions may make it possi-

ble for adatoms to migrate a long distance incorporated on the surface plane before converting back to an adatom. Paths A \rightarrow C and C \rightarrow C represent the long-distance diffusion mechanism. In the following, we discuss the diffusion behavior on the two surfaces.

For each hopping site on the W(110) surface, the four $\langle 111 \rangle$ hopping paths have identical migration barriers, and thus diffusion on the W(110) surface displays a two-dimensional character. As shown on the right panel of Fig. 7, biaxial strain causes an increase in the value of E_H^* , resulting in a degradation in the mobility of adatoms. Also, the MEP of a complete diffusion process of a $[\bar{1}11]$ -crowdion indicates that although a crowdion is highly mobile, its contribution to the diffusivity on the W(110) surface is negligible in a purely thermal environment due to the very high barrier for its formation. However, Henriksson *et al* observed the formation of $\langle 111 \rangle$ -crowdions during implantation of low-energy helium beams into tungsten⁵⁵, which is indicative of the presence of a diffusion mechanism that operates only under highly energetic conditions. It is therefore worth discussing A \rightarrow C and C \rightarrow C carefully.

As shown in Fig. 7, both $E_{A\rightarrow C}^*$ and $E_{C\rightarrow C}^*$ decrease as a result of equi-biaxial extension on the W(110) surface. The rectangular strain, $\varepsilon_{11} = -\varepsilon_{22} = -0.03$, also facilitates the long-distance diffusion since a $[\bar{1}11]$ -crowdion migrates without experiencing a significant energy barrier. Fig. 7 also shows that $E_{C\rightarrow C[\bar{1}11]}^*$ is always smaller than $E_{C\rightarrow A[\bar{1}11]}^*$. Therefore, long-distance diffusion on the W(110) surface is always possible, once a surface crowdion has already formed. However, the energy barrier can be easily modulated by an external biaxial strain. As an example, with $\varepsilon_{11} = -\varepsilon_{22} = 0.03$, $E_{C\rightarrow C}^*$ is only 40 meV lower than $E_{C\rightarrow A}^*$ and the $[\bar{1}11]$ -crowdion is suppressed from performing long-distance diffusion. With uniaxial compression, $\varepsilon_{22} = -0.03$, $E_{C\rightarrow A[\bar{1}11]}^* - E_{C\rightarrow C[\bar{1}11]}^*$ is 200 meV, and long-distance diffusion is expected to be enhanced.

Fig. 7 also illustrates the complicated nature of the diffusion process of the [100]-crowdion. The sign of $E_{C\rightarrow C[100]}^* - E_{C\rightarrow A[100]}^*$ changes, depending on the strain state: with $\varepsilon_{11} = \varepsilon_{22} = -0.03$ and $\varepsilon_{11} = -\varepsilon_{22} = -0.03$, $E_{C\rightarrow A[100]}^*$ is apparently lower, and the [100]-crowdion prefers to convert back to an adatom on a neighboring site. Thus, long-distance diffusion is suppressed. Compared with barriers of Path-H and Path-Ex, short-distance diffusion is the main mode of diffusivity on the W(001) surface, and the main mechanisms are Path-Ex and Path-A \rightarrow C. By contrast, for a strain-free surface, or a surface with an applied strain of $\varepsilon_{11} = \varepsilon_{22} = 0.03$, $E_{C\rightarrow C[100]}^*$ is lower. To gain an idea about the diffusion length scale, we estimate that, with $\varepsilon_{11} = \varepsilon_{22} = 0.03$, a [100]-crowdion on the W(001) surface will migrate approximately 100 Å before it converts to an adatom at 500 K. Long-distance diffusion is expected to be enhanced, and paths A \rightarrow C and C \rightarrow C are the dominant mechanisms of self-diffusion on the W(001) surface.

B. Mechanism Diagram

Though it is clear now that formation and migration of surface crowdions are the main diffusion mechanism on the W(001) surface in most cases, the preferred diffusion direction has not been fully discussed yet. Since crowdions on the W(001) surface migrate along either the [100] or the [010] direction, an applied external strain can induce anisotropy. To elucidate the directionality of diffusion in more details, we construct here a “mechanism diagram” for diffusion on the W(001) surface, as shown in Fig. 8. The diagram displays the dominant diffusion mechanism for a given range of applied strain.

Path-A \rightarrow C along [100] and [010] dominates surface diffusion, while Path-Ex is important only under extreme equi-biaxial compression. Fig. 8 also indicates that applying equi-biaxial strains is able to realize the transition of the major mechanism from Path-Ex to Path-A \rightarrow C. Since Path-Ex is at 45° to both [100] and [010] on the (001) surface, and formation of a [100]-crowdion or a [010]-crowdion has the same barrier with $\varepsilon_{11} = \varepsilon_{22}$, diffusion on the W(001) surface will not have preferential direction under equi-biaxial external strain. On the other hand, Fig. 8 shows symmetry with respect to the line $\varepsilon_{11} = \varepsilon_{22}$. Therefore, in the case of $\varepsilon_{11} \neq \varepsilon_{22}$, diffusion anisotropy will be promoted. Though the major surface diffusion mechanism is expected to be the formation and migration of surface crowdions, the primary diffusion direction will strongly depend on the pattern of externally applied biaxial strain. If one keeps ε_{11} constant and increases ε_{22} from negative to positive, diffusion mode will change from [100]-preferred to [010]-preferred after ε_{22} crosses the line $\varepsilon_{11} = \varepsilon_{22}$. Similarly, the transition from [010]-preferred to [100]-preferred is realizable by keeping ε_{22} constant while increasing ε_{11} instead. Together with discussions in Sec. IV A, we can comprehensively understand the picture of self-diffusion on the W(001) surface.

Combining Fig. 2 and Fig. 8, we should expect the existence of transition regions in which two or more mechanisms have approximately equal possibility to be taken. As an example, Fig. 8 presents a transition region between Path-Ex and Path-A \rightarrow C roughly estimated at 1000 K, which is determined by the condition: $\ln(0.1) < (E_{Ex}^* - E_{A\rightarrow C}^*)/k_B T < \ln(10)$, and the prefactor is assumed as a constant for all diffusion paths. This transition region mainly locates in the compression part and satisfies $\varepsilon_{11} \approx \varepsilon_{22}$. The accurate determination of transition regions, however, requires knowledge of the prefactor of each diffusion path as a function of bi-axial strain which is out of the scope of the current work.

C. Bonding Charge Density

To explain the small migration barriers of both crowdions, we present bonding charge density $\rho^{\text{bond}}(\mathbf{r})$ of [100]-crowdion on the W(001) surface and $[\bar{1}11]$ -crowdion on the W(110) surface in upper and lower panels of Fig. 9,

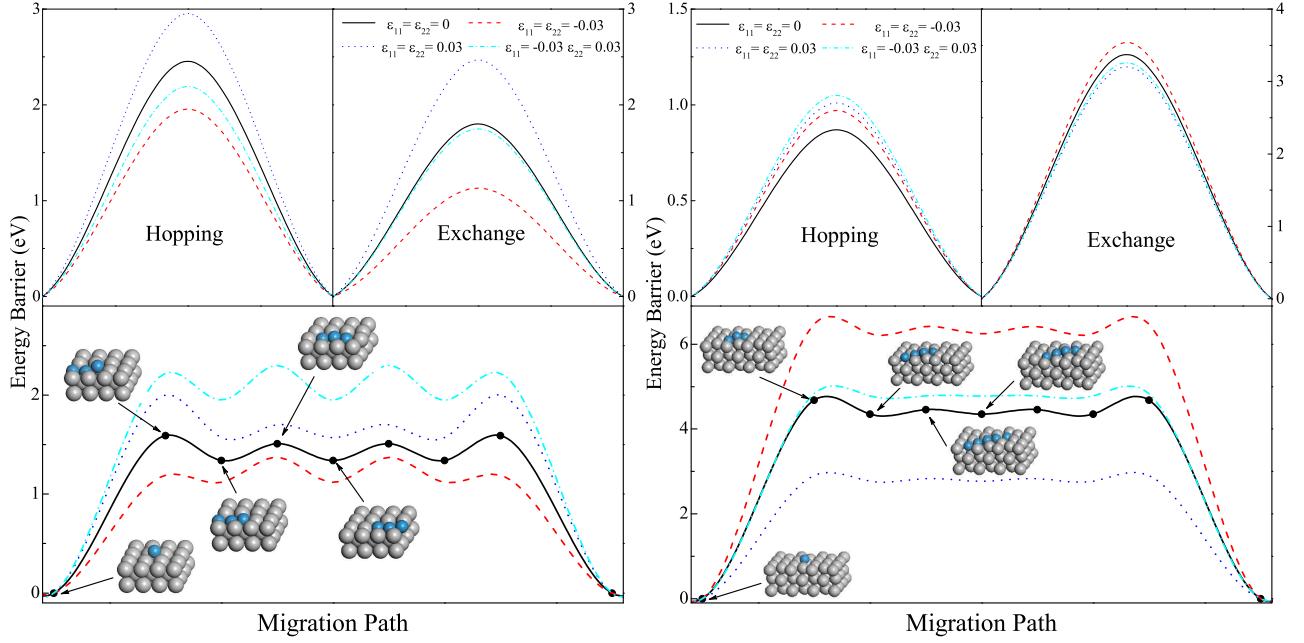


FIG. 7. MEPs of diffusion mechanisms under four different strain status: free strain, equi-biaxial extension, equi-biaxial compression, and rectangular strain. The left panel presents MEPs on the W(001) surface, and the right panel presents those on the W(110) surface. The lower part in each panel presents a schematic illustration of a complete process of a crowdion diffusion.

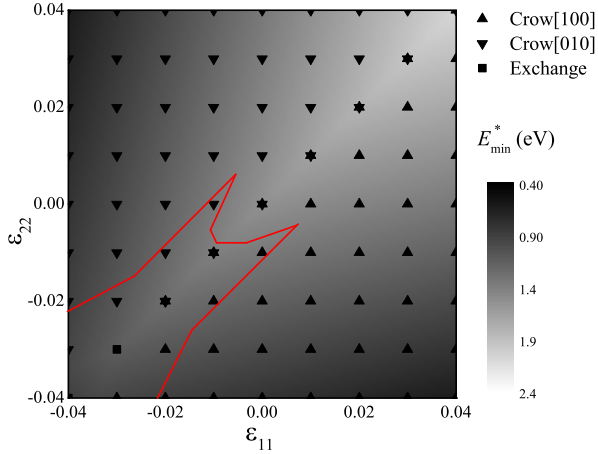


FIG. 8. Mechanism diagram for the dominant diffusion mechanisms on the W(001) surface. Symbols represent the diffusion path with the lowest energy barrier under a given strain status. The area surrounded by red (gray) lines is the transition region between Path-Ex and Path-ExC at 1000 K.

respectively. $\rho^{\text{bond}}(\mathbf{r})$ is defined as the difference between the total charge density of the system ρ and the superposition of isolated neutral atomic charge densities ρ_i^{atom} , placed at atomic sites

$$\rho^{\text{bond}}(\mathbf{r}) = \rho(\mathbf{r}) - \sum_i \rho_i^{\text{atom}}(\mathbf{r} - \mathbf{r}_i), \quad (6)$$

where \mathbf{r}_i is the position of the i -th atom. Therefore $\rho^{\text{bond}}(\mathbf{r})$ represents the net charge redistribution of the system.^{56,57} It is clear that these two oriented crowdions share several common characteristics: (1) the interplanar interaction is weak, (2) accumulating charge appears to be anisotropic; bonding has one-dimensional directionality, and (3) the crowdion pair shows a crowdion rather than a dumb-bell configuration. Therefore, both crowdion pairs have short migration distances and can glide within the surface layer. Furthermore, these characteristics of $\rho^{\text{bond}}(\mathbf{r})$ suggest that bonding anisotropy determines the migration anisotropy. Since $\rho^{\text{bond}}(\mathbf{r})$ on two surfaces are similar to each other, we only discuss $\rho^{\text{bond}}(\mathbf{r})$ of the $[\bar{1}11]$ -crowdion. Because $\rho^{\text{bond}}(\mathbf{r})$ accumulates along $[\bar{1}11]$, the migration path which deviates from $[\bar{1}11]$ will induce severe deformation of $\rho^{\text{bond}}(\mathbf{r})$, and is thus energetically unfavorable. On the other hand, if the migration path is along the $[\bar{1}11]$ direction, neither $\rho^{\text{bond}}(\mathbf{r})$ between two atomic layers nor $\rho^{\text{bond}}(\mathbf{r})$ will experience large disturbance. Consequently, $E_{\text{C} \rightarrow \text{C}[\bar{1}11]}^*$ is very low. Similar statements can be made for the $[100]$ -crowdion as well.

D. Dynamical Simulations

Up till now, discussions about the dynamics on surfaces are based on energetic scenarios of migration. In order to provide more direct evidence of the atomistic mechanisms of surface diffusion, we have performed *ab*

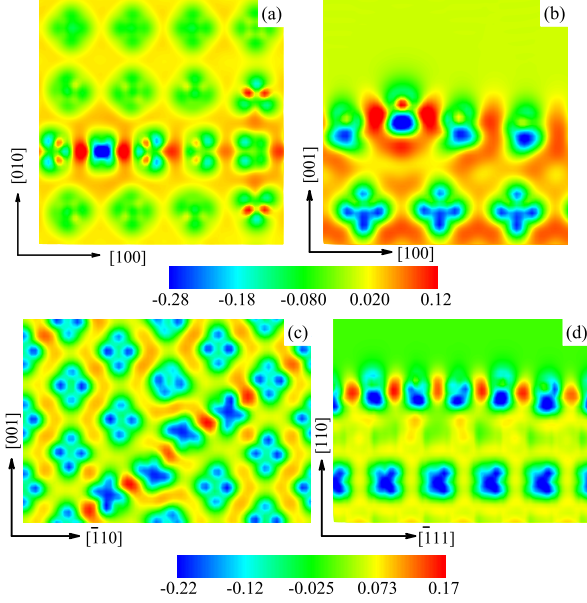


FIG. 9. (Color Online) Bonding charge density (in unit of $e/\text{\AA}^3$) of [100]-crowdion on the W(100) surface [(a) - a (100) slice, (b) - a (001) slice] and $\bar{1}11$ -crowdion on the W(110) surface [(c) - a (110) slice, (d) a $\bar{1}\bar{1}2$ slice].

initio molecular dynamics (AIMD) simulations on the W(001) surface. a [100]-crowdion is set on a 8×6 supercell. The temperature T is set to 800 K. Nosé-Hoover thermostat algorithm is employed to control T .⁵⁸ The total simulation period is 1.5 ps with 1000 AIMD steps. We observed that the [100]-crowdion moves 3 steps along the [100] direction and then converts back to an adatom, as shown in Fig. 10. This is direct evidence of the conversion mechanism discussed in Sec. IV A. Further, we also checked the path of crowdion-mediated exchange on the surface. In this AIMD simulation, T is set to 1100 K. The total simulation time is 1.5 ps. We did not observe the formation of a crowdion from an adatom. This is due to the high value of $E_{A \rightarrow C}^*$ and the short AIMD simulation period. Our preliminary AIMD results support the possibility and limitation of long-distance diffusion on the W(001) surface. One should note that high migration barriers on the W(001) surface make the direct observation of diffusion of adatoms difficult.

V. CONCLUSIONS

Employing first principles calculations of migration and formation energies, we have studied the effects of biaxial strains on atomic diffusion on the W(001) and the W(110) surfaces. By performing over 100 NEB calculations, we have accurately established the dependence of E_H^* , E_{Ex}^* , and $E_{A \rightarrow C}^*$ on externally applied biaxial strain. Our results indicate that the mechanisms of atomic diffusion are totally different on the (001) and (110) sur-

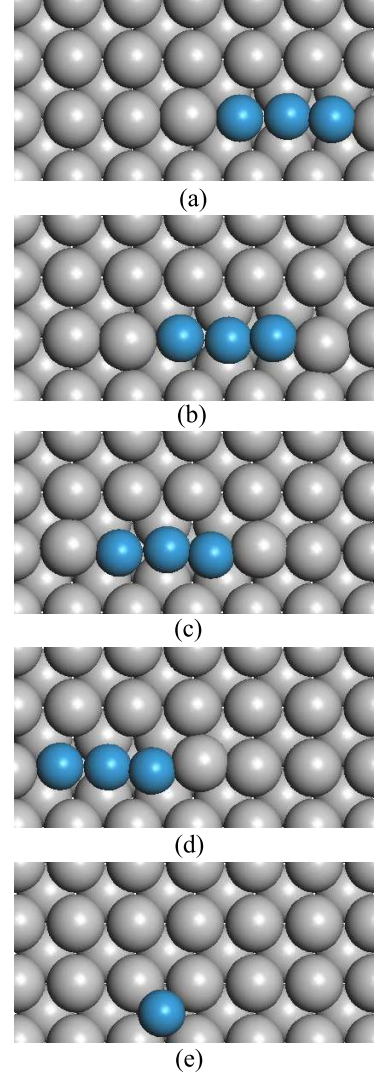


FIG. 10. (Color Online) Snapshots of the migration process of a [100]-crowdion on the W(001) surface. Atoms whose displacements are smaller than 0.4\AA have been projected to their crystallographic sites in order to make snapshots easier to read.

faces. While hopping is the main migration mechanism on the W(110) surface, the mechanism is unaffected by external loadings. Though $E_{A \rightarrow C}^*$ decreases quickly under equi-biaxial strain, it is still 2 eV higher than E_H^* even with $\varepsilon_{11} = \varepsilon_{22} = 0.03$. In contrast, the scenario of atomic diffusion on the W(001) surface is more complicated. The mechanism diagram based on $E_H^*(\varepsilon)$, $E_{Ex}^*(\varepsilon)$, and $E_{A \rightarrow C}^*(\varepsilon)$ demonstrates that not only the diffusion mechanism, but also the diffusion direction can be modulated by patterns of biaxial strains on the W(001) surface. By increasing the equi-biaxial loading where $\varepsilon_{11} = \varepsilon_{22}$, diffusion becomes isotropic, and the dominant mechanism transitions from the Path-Ex to the Path-A \rightarrow C mechanism. On the other hand, if the loading is anti-symmetric, where $\varepsilon_{11} = -\varepsilon_{22}$, diffusion will be

more anisotropic and the primary diffusion direction will change. However, the major mechanism remains as the formation and the movement of surface crowdions.

We further calculated $E_{C \rightarrow C[100]}^*$ on the W(001) and $E_{C \rightarrow C[\bar{1}11]}^*$ on the W(110) surfaces. These surface crowdions both show high mobility with low migration barriers (< 0.2 eV). They are also strongly anisotropic. By analyzing the bonding charge density, we found that both crowdions are nearly one-dimensionally bonded, and have weak inter-planar interaction. These features explain the high mobility and anisotropy of surface crowdions. Due to the essential contribution from Path-A \rightarrow C and the large difference between $E_{A \rightarrow C}^*$ and $E_{C \rightarrow C[100]}^*$, the diffusion on the W(001) surface should show an incubation period between fast movement of crowdions. On the other hand, since $[\bar{1}11]$ -crowdions have very high formation barrier, and thus can be generated only by ion bombardment, the high mobility indicates that diffusion on the W(110) surface diffusion is important only under plasma or ion bombardment conditions.

Finally, we studied crowdion-adatom conversion under biaxial strain. Results show that the barrier of the conversion $E_{C \rightarrow A}^*$ is comparable to the migration bar-

rier $E_{C \rightarrow C}^*$ on both surfaces. Under zero strain, surface crowdions on both surfaces prefer to migrate multiple steps before they convert to adatoms. More importantly, $E_{C \rightarrow A}^*$ and $E_{C \rightarrow C}^*$ have different dependence on strain. As a consequence, based on the values of applied strain components, the long distance diffusion of a crowdion will be enhanced or suppressed. Since crowdions are important carriers of surface diffusion in plasma-facing materials, external strain will be important to the evolution of surface morphology. Therefore, the present results are expected to be of fundamental importance to the dynamical modeling of tungsten surface evolution.

ACKNOWLEDGMENTS

The authors are grateful to Drs. G. Po and T. Crosby, and Mr. D. Rivera for their inspiring discussions. This work is supported by the Air Force Office of Scientific Research (AFOSR), award number FA9550-11-1-0282 with UCLA, and with partial support from the Department of Energy (DOE), Office of Fusion Energy Sciences through grant number DE-FG02-03ER54708:014.

-
- ¹ W. Xiao, P. Greaney, and D. C. Chrzan, Phys. Rev. Lett. **90**, 156102 (2003).
 - ² W. Xiao, P. Greaney, and D. C. Chrzan, Phys. Rev. B **70**, 033402 (2004).
 - ³ Z. Duan and W. Xiao, Surf. Sci. **604**, 337 (2010).
 - ⁴ M. J. Aziz, Y. Zhao, H. Gossmann, S. Mitha, S. P. Smith, and D. Schiferl, Phys. Rev. B **73**, 054101 (2006).
 - ⁵ R. Zhu, E. Pan, and P. W. Chung, Phys. Rev. B **75**, 205339 (2007).
 - ⁶ R. Panat, K. J. Hsia, and D. G. Cahill, J. Appl. Phys. **97**, 013521 (2005).
 - ⁷ M. Mavrikakis, B. Hammer, and J. K. Nørskov, Phys. Rev. Lett. **81**, 2819 (1998).
 - ⁸ P. H. Dederichs and K. Schroeder, Phys. Rev. B **17**, 2524 (1978).
 - ⁹ J. A. Thornton and D. W. Hoffman, Thin Solid Films **171**, 5 (1999).
 - ¹⁰ H. J. Gao, J. Mech. Phys. Solids **42**, 741 (1994).
 - ¹¹ A. Haasz, M. Poon, and J. W. Davis, J. Nucl. Mater. **266-269**, 520 (1999).
 - ¹² R. A. Causey, J. Nucl. Mater. **300**, 91 (2002).
 - ¹³ G. A. Cottrell, J. Nucl. Mater. **334**, 166 (2004).
 - ¹⁴ D. M. Goebel and I. Katz, *Fundamentals of Electric Propulsion: Ion and Hall Thrusters*, Vol. 1 (Wiley, 2008).
 - ¹⁵ W. Shu, A. Kawasuso, and T. Yamanishi, J. Nucl. Mater. **386-388**, 356 (2009).
 - ¹⁶ S. K. Das, M. Kaminsky, and G. Fenske, J. Nucl. Mater. **76**, 215 (1978).
 - ¹⁷ K. Tokunaga, O. Yoshikawa, K. Makise, and N. Yoshida, J Nucl Mater **307**, 130 (2002).
 - ¹⁸ S. Lindig, M. Balden, V. Kh Alimov, T. Yamanishi, W. Shu, and J. Roth, Phys. Scr. **T138**, 014040 (2009).
 - ¹⁹ S. J. Zinkle, Nucl. Instr. Meth. B **286**, 4 (2012).
 - ²⁰ K. L. Wilson, Nucl. Fusion Special Issue: International Atomic Energy Agency, Vienna, 28 (1984).
 - ²¹ M. Tokitani, N. Yoshida, K. Tokunaga, H. Sakakita, S. Kiyama, H. Koguchi, Y. Hirano, and S. Masuzaki, J. Plasma Fusion Res. **5**, 12 (2010).
 - ²² W. Wang, J. Roth, S. Lindig, and C. H. Wu, J. Nucl. Mater. **299**, 124 (2001).
 - ²³ F. Dausinger and H. Schultz, Phys. Rev. Lett. **35**, 1773 (1975).
 - ²⁴ T. Amino, K. Arakawa, and H. Mori, Phil. Mag. Lett. **91**, 86 (2010).
 - ²⁵ L. Chen, Y. Liu, H. Zhou, S. Jin, Y. Zhang, and G. Lu, Sci. China **55**, 614 (2012).
 - ²⁶ D. Nguyen-Manh, A. P. Horsfield, and S. L. Dudarev, Phys. Rev. B **73**, 020101 (2006).
 - ²⁷ P. M. Derlet, D. Nguyen-Manh, and S. L. Dudarev, Phys. Rev. B **76**, 054107 (2007).
 - ²⁸ L. Ventelon, F. Willaime, C. C. Fu, M. Heran, and I. Ginoux, J. Nucl. Mater. **425**, 16 (2012).
 - ²⁹ C. S. Becquart and C. Domain, Phys. Rev. Lett. **97**, 196402 (2006).
 - ³⁰ S. Y. Davydov and S. K. Tikhonov, Surf. Sci. **371**, 157 (1997).
 - ³¹ J. Yang, W. Hu, and J. Tang, J. Phys.: Condens. Matter **23**, 395004 (2011).
 - ³² D. Chen, W. Hu, H. Deng, L. Sun, and F. Gao, Eur. Phys. J. B **68**, 479 (2009).
 - ³³ G. Antczak and G. Ehrlich, Phys. Rev. Lett. **92**, 166105 (2004).
 - ³⁴ P. G. Flahive and W. R. Graham, Surf. Sci. **91**, 449 (1980).
 - ³⁵ W. Xu and J. B. Adams, Surf. Sci. **319**, 58 (1994).
 - ³⁶ P. J. Feibelman, Phys. Rev. Lett. **65**, 729 (1990).
 - ³⁷ R. C. Pasianot, A. M. Monti, G. Simonelli, and E. J. Savino, J. Nucl. Mater. **276**, 230 (2000).
 - ³⁸ S. Han, L. A. Zepeda-Ruiz, G. J. Ackland, R. Car, and

- D. J. Srolovitz, Phys. Rev. B **66**, 220101(R) (2002).
- ³⁹ L. A. Zepeda-Ruiz, J. Rottler, S. Han, G. J. Ackland, R. Car, and D. J. Srolovitz, Phys. Rev. B **70**, 060102 (2004).
- ⁴⁰ D. Iotova, N. Kioussis, and S. P. Lim, Phys. Rev. B **54**, 14413 (1996).
- ⁴¹ G. Kresse and J. Hafner, Phys. Rev. B **47**, 558 (R) (1993).
- ⁴² G. Kresse and J. Furthmüller, Phys. Rev. B **54**, 11169 (1996).
- ⁴³ J. P. Perdew, K. Burke, and M. Ernzerhof, Phys. Rev. Lett. **77**, 3865 (1996).
- ⁴⁴ P. E. Blöchl, Phys. Rev. B **41**, 5414 (1990).
- ⁴⁵ H. J. Monkhorst and J. D. Pack, Phys. Rev. B **13**, 5188 (1976).
- ⁴⁶ D. J. Shu, F. Liu, and X. G. Gong, Phys. Rev. B **64**, 245410 (2001).
- ⁴⁷ M. C. Tringides, *Surface Diffusion: Atomistic and Collective Processes*, Vol. 360 (Springer, 1997).
- ⁴⁸ J. P. Hirth and J. Lothe, *Theory of Dislocations* (McGraw-Hill, New York, 1968) pp. 761–762.
- ⁴⁹ G. Henkelman and H. Jónsson, J. Chem. Phys. **115**, 9657 (2001).
- ⁵⁰ D. Sheppard, R. Terrell, and G. Henkelman, J. Chem. Phys. **128**, 134106 (2008).
- ⁵¹ T. D. de la Rubia, R. S. Averback, R. Benedek, and W. E. King, Phys. Rev. Lett. **59**, 1930 (1987).
- ⁵² G. L. Kellogg, T. T. Tsong, and P. Cowan, Surf. Sci. **70**, 485 (1978).
- ⁵³ C. Chen and T. T. Tsong, Phys. Rev. B **41**, 12403 (1990).
- ⁵⁴ G. Antczak and G. Ehrlich, *Surface Diffusion: Metals, Metal Atoms and Clusters* (Cambridge University Press, 2010).
- ⁵⁵ K. Henriksson, K. Nordlund, J. Keinonen, D. Sundholm, and M. Patzschke, Phys. Scr. **T108**, 95 (2004).
- ⁵⁶ S. Sun, N. Kioussis, S.-P. Lim, A. Gonis, and W. Gourdin, Phys. Rev. B **52**, 14421 (1995).
- ⁵⁷ Z. Z. Chen and C. Y. Wang, Phys. Rev. B **72**, 104101 (2005).
- ⁵⁸ S. Nosé, J. Chem. Phys. **81**, 511 (1984).